Liquid Argon Purity Monitor Concept

Christopher Hopp
Mentor: Emilija Pantic, PhD
Department of Physics and Astronomy - University of California - Davis

High purity liquid argon is utilized in time projection chambers (TPCs), for both neutrino and weakly-interacting massive particle (WIMP) dark matter detection experiments. These detectors search for interactions between incident particles and the argon nuclei. The resulting collisions would be characterized by a signature of emitted photons and freed electrons. Maintaining high liquid argon purity levels is critical to the function of the detector as electronegative impurities can capture the freed electrons in the drift region. Following is a design for a purity monitor to be implemented in a test stand for the DarkSide-20k dark matter experiment.

I. INTRODUCTION

For nearly 90 years, astronomers and physicists have known that there is more than meets the eye when it comes to the composition of our universe. Beginning in the early 1930's with the work of Oort and Zwicky, strange phenomena have been observed in rotating galaxies[1,2]. The luminous matter that we are able to observe with our telescopes is not able to account for the velocity of the stars in the outer bands of spiral galaxies. Instead, the matter density of these galaxies must greatly exceed that produced by luminous matter alone as shown in FIG. 1. In 1980, it was shown by Vera Rubin and Kent Ford, with overwhelming evidence, that there was some missing type of matter throughout our universe[3].

There are many theories about the potential nature of a dark matter particle. One of the leading candidates is the Weakly Interacting Massive Particle, or WIMP. This particle is predicted by models of physics beyond the Standard Model in order to solve other problems in physics, but happens to fit the requirements of a dark matter particle. One of the strongest pieces of theoretical evidence in support of the WIMP as dark matter is that if we examine predictions of the density of dark matter in the early universe and extrapolate those predictions forward in time, we arrive independently at the current dark matter density of the universe[4].

While dark matter doesn't interact with ordinary matter via the electromagnetic force, WIMPs are predicted to interact with ordinary matter at or below the weak scale. This gives us a potential method of detecting these particles using technology currently available. One of the primary detection methods is the use of a cryogenic noble liquid as a target nucleus. Incoming dark matter particles would collide with these nuclei, producing a shower of photons and electrons. These emissions could then be used to reconstruct the event and provide information on the properties of the dark matter particle. The DarkSide experiment at Gran Sasso National Lab uses liquid argon in a two-phase time projection chamber to search for these collisions[5].

Liquid noble time projection chambers require high-purity, low-noise target media. In the case of liquid argon, underground argon sources help to reduce backgrounds from radioactive decays, but impurity in the argon can still exist. Detector elements can also outgas, adding to the level of impurity. To quantify these effects, a purity monitor is necessary to track the level of impurity in the detector. Following is a design and for a liquid argon purity monitor to be implemented in a high-voltage test stand for the DarkSide-20k experiment as part of Dr. Pantic's group.

II. THEORY

The most concerning impurities present in liquid argon are electronegative molecular and atomic species, most commonly oxygen. These species have a high affinity for electrons and can thus capture any drifting electrons produced in a collision event. This capture of electrons effectively diminishes any potential signal, decreasing the signal to noise ratio. For an electron capture process by an electronegative impurity, $\mathrm{e}^- + \mathrm{S} \xrightarrow{\mathrm{k}_s} \mathrm{S}^-$ the rate constant k_s is defined as

$$k_s = \int v\sigma(v)f(v)\,dv \tag{1}$$

where v is the instantaneous velocity of the drift electron, $\sigma(v)$ gives the capture reaction cross-section, and $f(v)$ is the Maxwell velocity distribution.

As electrons drift through the argon volume and are captured by impurities, their number, N, decreases according to

$$\frac{\mathrm{d}N}{\mathrm{d}t} = -k_s N_s N \tag{2}$$

Assuming the number of impurities, N_s, does not change with time, Eq. (2) can be integrated to obtain the number of electrons present as a function of time

$$N(t) = N_0 \mathrm{e}^{-t/\tau} \tag{3}$$

The associated time constant, $\tau = \frac{1}{k_s N_s}$, can be used to calculate the concentration of impurity present.

The impurity concentration is given as

$$\rho = \frac{N_s}{N_{Ar}} = \frac{1}{k_s N_{Ar}} \frac{1}{\tau} \tag{4}$$

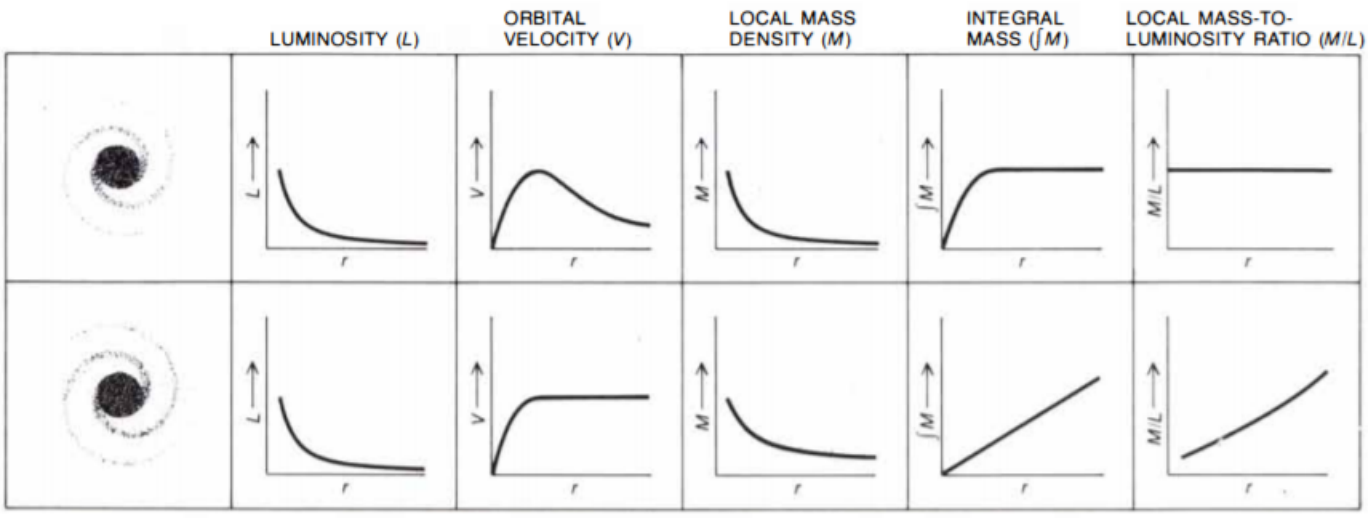

FIG. 1: Hypothetical(upper) and actual(lower) galactic rotation curves demonstrating orbital velocity does not decrease with luminosity and, thus, total mass extends beyond the luminous galactic center.[6]

N_{Ar} can be determined by the density and molar mass of argon while k_s depends on the specific species of impurity. Oxygen is the primary electronegative species involved in electron capture. Using the rate constant for electron attachment of oxygen in argon gives a measure of oxygen equivalent impurity[7]. With numeric values of N_{Ar} and k_s, Eq. (4) ultimately yields an expression for impurity concentration given an electron lifetime[8].

The general operation of a purity monitor is to produce free electrons at a cathode within an argon volume. Those electrons are then drifted in an electric field to an anode. During this drift period, some of the electrons will be captured by the impurities in the argon. Both the anode and cathode are connected to a charge sensitive preamplifier that measures the change in charge due to electrons released at the cathode and collected at the anode. The drift region is shielded by two mesh grids to ensure that the preamplifier detects only the charges due to collection of electrons, and not induced effects during their drift through the argon volume. This divides the purifier into three distinct regions, the cathode, drift, and anode. The purity monitor is able to measure the charge produced at the cathode, charge received at the anode, and time in each region. From these values, an electron lifetime can be calculated.

These regions and associated charges measured by the amplifier are illustrated in FIG. 2. As electrons are released from the cathode, the total charge detected increase to a maximum $Q_{cathode}$. As the electrons drift toward the anode, the amplifier is shielded by the mesh grids and charge sensed remains constant. Once the electrons pass through the upper grid to the cathode, the total charge falls to Q_{anode}. The difference between $Q_{cathode}$ and Q_{anode} represents the amount of electrons captured by impurity. The time spent in each region is also measured by the amplifier.

In order to calculate this lifetime, a relationship between these observed values and lifetime is developed. The instantaneous current as the flow of electrons crosses the mesh shielding grid can be expressed in terms of the velocity of the electrons as

$$I(t) = N(t)e\frac{v}{d} \tag{5}$$

where the charge is given by the product of the number of electrons $N(t)$ and their individual charge e. Because velocity of the electrons is taken to be constant in each individual region and the distance is fixed by the geometry, expressing as Eq. (5) shows the time dependence of the current lies exclusively in the number of charges. In general, current can be expressed as $I(t) = \frac{\mathrm{d}Q(t)}{\mathrm{d}t}$. Begin-

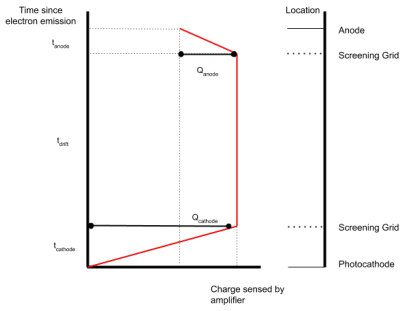

FIG. 2: Drift time with charged sensed by the amplifier given in red[8]

ning at the cathode, Eq. (5) can be integrated to produce an expression for charge

$$Q_C = \int_0^{t_C} N(t) e \frac{v}{d_C}\, dt \tag{6}$$

Substituting Eq. (3) and taking the constant velocity term out of the integral yields

$$Q_C = N_0 e \frac{v}{d_C} \int_0^{t_C} \mathrm{e}^{-t/\tau}\, dt \tag{7}$$

Performing the integration and recognizing $Q_0 = N_0 e$ and $\frac{v}{d_C} = t_C$ gives a final expression for charge at the cathode

$$Q_c = \frac{Q_0 \tau}{t_C} \left(1 - \mathrm{e}^{-t_C/\tau}\right) \tag{8}$$

The same process can be applied at the anode. However, as the electrons drift through the argon volume their number will decrease according to Eq. (3). The number of electrons remaining at the anode grid, then, is given by their decrease across the cathode and drift regions $N_A = N_0 \mathrm{e}^{-t_C/\tau} \mathrm{e}^{-t_D/\tau}$. The charge detected at the anode is then

$$Q_A = \frac{Q_0 \tau}{t_A} \left(1 - \mathrm{e}^{-t_A/\tau}\right) \mathrm{e}^{-t_C/\tau} \mathrm{e}^{-t_D/\tau} \tag{9}$$

By measuring the fraction of electrons that were produced at the cathode and are received at the anode, we can quantify the amount of impurity present in the argon. The electron lifetime given in Eq. (3) can then be determined from the ratio of charge at the anode, Eq. (9), to charge at the cathode, Eq. (8), $R = \frac{Q_A}{Q_C}$ and electron drift times by[9]

$$\tau = -\frac{1}{\ln R} \left(t_D + \frac{t_A + t_C}{2}\right) \tag{10}$$

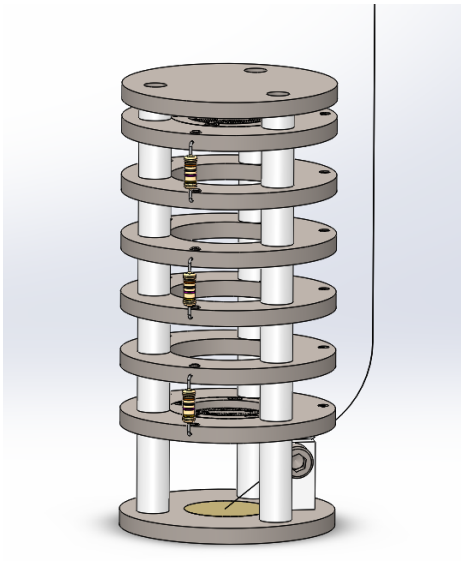

FIG. 3: LAr purity monitor SolidWorks model

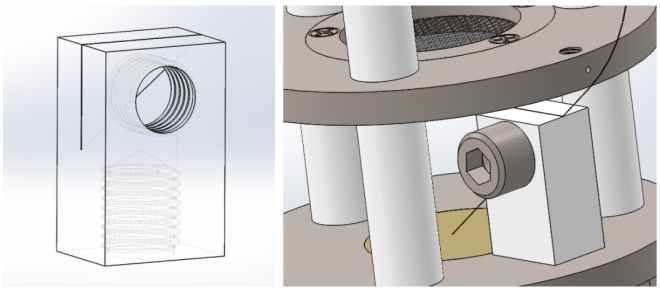

FIG. 4: Fiber optic assembly

Combining Eq. (10) with the expression for impurity concentration in Eq. (4) gives a relationship between impurity concentration and purity monitor data. Ultimately, the design presented aims to achieve a sensitivity to electron lifetimes on the order of μs.

III. DESIGN

The purity monitor presented in FIG. 3 was designed in SolidWorks. The monitor utilizes a photocathode coupled to a xenon flashlamp as an electron source via the photoelectric effect. These electrons drift through a uniform electric field established by the field shaping rings and resistor chain. The charges are detected leaving the cathode and arriving at the anode by a charge sensitive preamplifier.

While relatively simple in theory, design of the purity monitor was much more complicated. A gold photocathode with a work function of 5.1 eV was chosen as the electron source. Gold was selected for its favorable anti-corrosion and electrical conductivity properties. The electrons are liberated using an external xenon flashlamp coupled to a 100 micron silica fiber. To optimize the location of the freed electrons, the fiber was placed at a 33° angle to the horizontal. This maintains the fiber in a maximally vertical position while ensuring that the fiber does not physically overshadow any of the drifting electrons. This placement creates an illuminated patch on the order of $10^{-2}\,\mathrm{mm}^2$ in the center of the photocathode. If the fiber were placed at too shallow an angle, the light would not be confined to this central location. This could create free electrons outside of the drift region of the purity monitor where they could be lost to diffusion. If the fiber is placed at too steep of an angle, it will physically impede the flow of electrons towards the anode. The installation of the fiber optic is demonstrated in FIG.4.

Once the electrons are liberated, they are drifted through a uniform electric field to the anode. This electric field is established by a series of stainless steel rings connected via a resistor chain, establishing a constant electric field. The photocathode is set at a potential of -610 volts while the anode is set at positive 5000 volts. In an ideal case, the preamplifier would sense only the

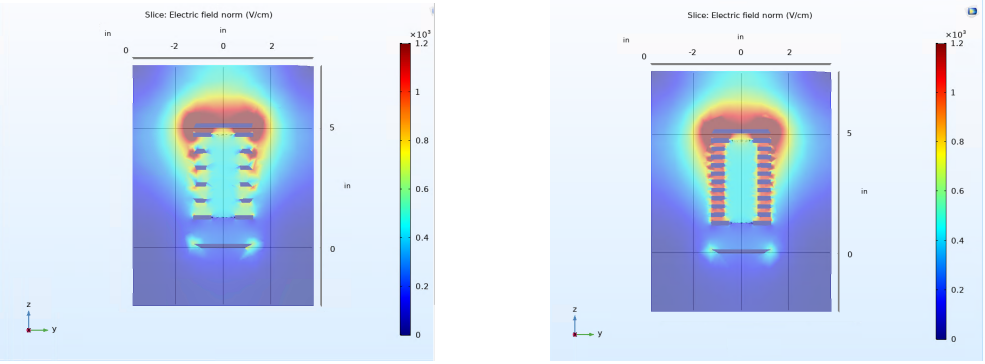

(a) Midline slice with five field shaping rings (b) Midline slice with nine field shaping rings

FIG. 5: COMSOL electric field simulations

charges being removed from the cathode and absorbed at the anode, and not be affected by any induced charges due to the electron drift. This provides a method for determining the time for the electrons to drift through each of the three field regions. To achieve this signal, Frisch screening grids were installed immediately after the cathode and immediately prior to the anode. These two grids are capacitively held at a constant potential, independent of drifting charges, such that the field between them also remains constant.

While the shield grids are effective at shielding the amplifier from induced charges within the volume, they could potentially interfere with the drift path of the electrons. To remedy this, the grids are sized and the electric fields are designed in such a manner to achieve 100% transparency to the drifting electrons. If the electric field in the region after the shield grid is sufficiently stronger than the field in the region before the grid, electrons will be forced through the screening grid, rather than attracted to it. This is achieved by fields in neighboring regions having the relationship

$$\frac{E_A}{E_B} \geq \frac{1+\rho}{1-\rho}\left[\frac{1+\frac{a}{4\pi D_A}\left(\rho^2-4\ln\rho\right)}{1+\frac{a}{4\pi D_B}\left(\rho^2-4\ln\rho\right)}\right] \tag{11}$$

where the electric fields before and after the grid are represented E_B and E_A respectively, D_A and D_B give the length of the region, and grid pitch is given as a. The wire density, ρ, is defined as $\frac{2\pi r}{a}$ for parallel wire configurations[10]. This design uses a grid mesh, so the wire density must be doubled[11]. With a wire diameter of 10 microns and grid pitch of 500 microns, the electric fields must increase in strength by a factor of 2 in each region of the monitor. The field strength and spacing was designed to produce this effect and then simulated using COMSOL Multiphysics software.

As evident by the electric field simulation illustrated in FIG. 5a, the electric fields produced are approximately 250, 500, and 1000 V/cm at the cathode, drift, and anode regions, respectively. As a design revision, the number of field shaping rings was increased to nine. The same study was again performed and is shown in FIG. 5b. The relative strength of the fields remained the same, however, the edges of the drift region are more pronounced. This will ultimately produce a more uniform drift region.

The field shaping rings are separated by spacers made of polyether ether ketone (PEEK). This serves as an electrical insulator between the components, so the only connection between the individual rings are the resistors. These resistors are sized so that the voltage changes linearly through the series of shaping rings. Each pair of field shaping rings creates its own electric field with strength $E = \frac{V}{d}$. With uniform spacing between field rings in the drift region, to create a uniform field the potential difference between the rings must also be uniform. In the cathode and anode regions, the distance between the rings is different from the distance between rings in the drift region. This helps to create the desired electric field ratios given by Eq. (11) while simultaneously maintaining a maximum potential of +5000 V at the anode and grounding the cathode shield grid.

These shield grids are shown in FIG. 6. The mesh itself is commercially available high-transparency stainless steel. This mesh is cut to fit and mounted in a stainless steel ring, machined with a recessed ledge to support

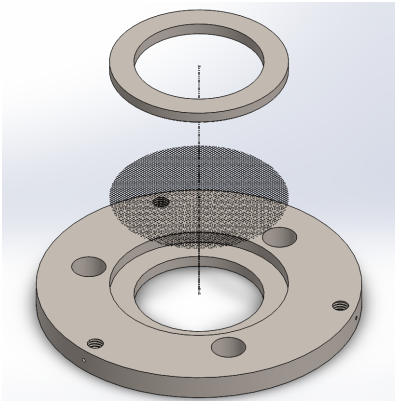

FIG. 6: Exploded view of shield grid assembly

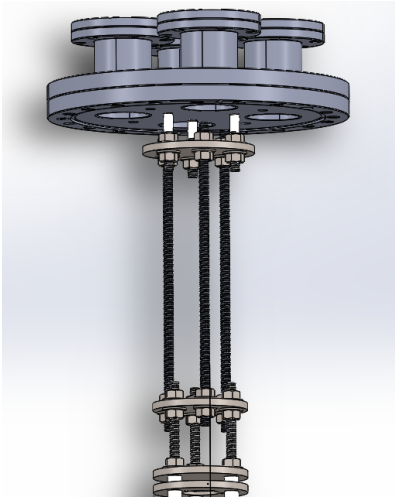

FIG. 7: Mounting assembly attached to cryostat flange

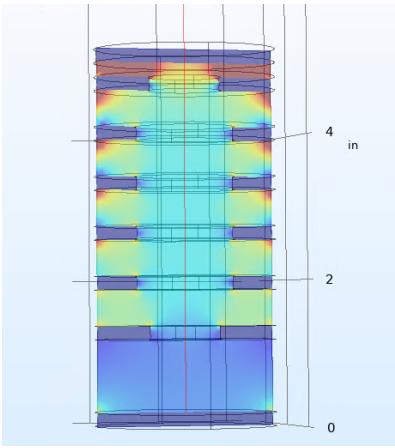

FIG. 8: Particle track for a single electron shown in red

the mesh. A second stainless steel ring is press fit on top of the mesh, holding it in place.

The entire apparatus is suspended in a liquid argon cryostat, as shown in FIG.7. Three short threaded PEEK rods connect the cryostat flange to a mounting plate supporting the purity monitor. These rods serve to thermally insulate the argon volume from the cryostat flange. The cryostat has both liquid and gas phase argon, so three longer stainless steel rods are used to suspend the purity monitor completely submerged in the liquid argon. Electrical and fiber-optic feedthroughs in the flange of the cryostat provide connections for the optical fiber and necessary power supply.

IV. STATUS

Physical work on the purity monitor was halted due to COVID-19 restrictions, however design revisions and further simulations are ongoing. Next steps will be to further tune the electric fields in the drift region of the monitor. The electric field strength will be increased to ultimately produce field strengths up to 1275 V/cm. This will result in a purity monitor with more field shaping rings that are thinner and decreased spacing between the rings. The resistor chain will have to be installed at an angle to allow for decreased ring spacing. A new SolidWorks model will have to be built to incorporate this design change and will eventually be used for manufacturing.

COMSOL simulations will also be done to simulate particle tracking through the monitor. One of these studies is illustrated in FIG.8. Studying these particle tracks will confirm the uniformity of the electric fields as well as the transparency of the screening grids.

With lab activities beginning to resume, construction of the purity monitor is expected to occur in early 2021 with testing to follow. Ultimately, a sensitivity to electron lifetimes on the order of μs is expected.

V. ACKNOWLEDGMENTS

Thank you to US Department of Education Ronald E. McNair Post-Baccalaureate Achievement Program for their continued support and a special thank you to all of the members of Pantic Group for all of their advice and guidance.

[1] J. H. Oort, Bulletin of the Astronomical Institutes of the Netherlands **6**, 249 (1932).
[2] F. Zwicky, Helv. Phys. Acta **6**, 138 (1933).
[3] V. C. Rubin, W. K. Ford Jr, and N. Thonnard, The Astrophysical Journal **238**, 471 (1980).
[4] G. Jungman, M. Kamionkowski, and K. Griest, Physics Reports **267**, 195 (1996).
[5] G. Zuzel, P. Agnes, I. Albuquerque, T. Alexander, A. Alton, D. Asner, H. Back, B. Baldin, K. Biery, V. Bocci, *et al.*, in *International Conference on Particle Physics and Astrophysics* (2017).
[6] V. C. Rubin, Scientific American **248**, 96 (1983).
[7] G. Bakale, U. Sowada, and W. F. Schmidt, The Journal of Physical Chemistry **80**, 2556 (1976).
[8] L. Tvrznikova, *Sub-GeV dark matter searches and electric field studies for the LUX and LZ experiments*, Ph.D. thesis, Yale University (2019).
[9] G. Carugno, B. Dainese, F. Pietropaolo, and F. Ptohos, Nuclear Instruments and Methods in Physics Research Section A: Accelerators, Spectrometers, Detectors and Associated Equipment **292**, 580 (1990).
[10] O. Bunemann, T. Cranshaw, and J. Harvey, Canadian journal of research **27**, 191 (1949).

[11] R. Bevilacqua, A. Göök, F.-J. Hambsch, N. Jovančević, and M. Vidali, Nuclear Instruments and Methods in Physics Research Section A: Accelerators, Spectrometers, Detectors and Associated Equipment **770**, 64 (2015).